American Flame Research Committee
2024 Symposium
Calgary, Alberta
September 30-October 03, 2024

Viability and robustness of video imaging spectro-radiometry (VISR) for estimating flare combustion efficiency

A. Kaveh[1,*], P. Lapeyre[1], J. C. Spinti[2] and K. J. Daun[1]

[1]*Department of Mechanical and Mechatronics Engineering, University of Waterloo, 200 University Ave W, Waterloo, ON, Canada, N2L 3G1*

[2]*Department of Chemical Engineering, University of Utah, Salt Lake City, UT, United States of America, 84112*

Abstract

This paper discusses the capability of video imaging spectro-radiometry (VISR) for measuring flare combustion efficiency (CE)/destruction removal efficiency (DRE) of methane. While this technique has been assessed experimentally in the literature, we examine its performance using computational fluid dynamics simulations of assisted flares in crosswinds, using a simplified three-channel version of the technique. Our analysis focuses on three points: (*i*) the veracity of the inferred local (pixel-wise) CE; (*ii*) the accuracy of the flare global CE estimates; and (*iii*) the ability of the VISR instrument to quantify stripped methane. The results indicate that the simplified VISR imaging approach provides accurate local CE estimates. On the other hand, the VISR global CE inference model lacks a physical basis, produces biased estimates and cannot accurately measure stripped methane.

Introduction

Flaring is often used to convert excess and unwanted hydrocarbon (HC) gases into carbon dioxide (CO_2) and water vapor (H_2O), which have significantly lower global warming potentials [1]. Flaring performance is often defined by combustion efficiency (CE), which is the portion of the carbon in the flare fuel stream that transforms into CO_2, or the destruction removal efficiency (DRE), which considers the fraction of a particular hydrocarbon species that is converted into CO_2. In the case of upstream oil and gas extraction, there is a particular focus on the methane (CH_4) contained in associated gas, due to its large global warming potential and emerging regulations [2,3].

While flaring is often assumed to have a CE or DRE close to 98% [4], in some circumstances, this figure may be significantly lower due to aerodynamic fuel stripping in crosswinds [5,6], steam and air assistance for smoke suppression [7–9], and the low heating value (HV) of fuel gaseous components [5,6,9–11]. Accordingly, diagnostics are urgently needed to assess the true impact of flaring on climate change, identify problematic operating conditions, and enforce environmental regulations.

Passive Fourier transform infrared spectrometry (PFTIR) is one of the main techniques for assessing flare CE [12–14]. In this approach, CE is inferred based on spectrally resolved emission measurements made using an open-path FTIR along a line-of-sight through the plume, typically one flame length downwind of the visible flame tip. However, PFTIR-derived CE estimates are sensitive to measurement location and do not account for plume heterogeneity. The emergence of commercial multispectral and hyperspectral mid-wavelength (MWIR) and long-wavelength (LWIR) infrared imagers, including light field (plenoptic) cameras [15], dispersive line-scan cameras [16], and imaging Fourier transform spectrometers (IFTSs) [17,18], provide a means to capture the transient development of the entire plume region with temporal, spatial, and spectral resolution, enabling the inference of the species column density and plume gas temperature distribution along each pixel light-of-sight (LOS).

Light field and line scan cameras provide significantly higher temporal resolution compared to IFTSs, albeit with significantly lower spectral resolution. In 2012 Zeng et al. [16] proposed the “video imaging spectro-radiometry” (VISR) technique based on a four-channel light field imager with three of the channels focused on key absorption features of CH_4 (3.2–3.4 μm), CO_2 (4.2–4.4 μm), and CO (4.5–4.9 μm), with an additional transparent window for

* Corresponding author: a3kaveh@uwaterloo.ca

capturing the ambient background radiance and broadband particulate emission. This approach was implemented into a commercial line-scan camera equipped with 42 uniformly-spaced spectral channels within the 2–5 μm spectrum [19], and later commercialized as the FlareGuardian™ remote sensing system, using a similar number of channels distributed between 3–5 μm [20]. The radiometric model used in the VISR approach is derived from simplifications and approximations to the radiative transfer equation (RTE) to connect the relative intensities measured over each pixel to a local "pixel-wise" CE estimate. Finally, a global CE is computed by averaging the local CE values of the pixels within a region-of-interest (ROI) that envelopes but excludes the visible flame. Although VISR flare CE estimates acquired through field trial experiments of steam- and air-assisted flares were consistent with those obtained through simultaneous extractive measurements [19,20], there remain unresolved questions as to the validity of the instrument model, and whether this technique can detect and quantify unburned fuel pockets that may be significantly colder than the rest of the flare plume. Notably, the manufacturer of this product claims that the CE may be found with "1% accuracy". Can this claim be correct?

This study conducts a numerical assessment of a simplified version of the VISR approach [16], based on the original four-band multispectral imaging method, to evaluate the feasibility of this technique for remote flare performance measurements. In this analysis, synthetic VISR broadband images are generated using temperature and species concentration fields obtained from computational fluid dynamics-large eddy simulation (CFD-LES) datasets of a steam-assisted industrial flare operating under varying crosswind conditions [21,22]. The results support the RTE simplifications applied to the VISR radiometric model and the accuracy of the inferred local CE but call into question the algorithm used to calculate global CE as well as the VISR instrument's capability in quantifying slipped (cold) fuel, which can represent a significant fraction of HC emissions under certain circumstances.

Flaring combustion efficiency

Combustion efficiency is defined as the fraction of carbon in the fuel stream supplied to the flare that is converted into CO_2. In many scenarios, the fuel composition and flow rate may not be known, in which case the carbon flow rate entering the flare may be inferred through a mass balance of carbon-containing species within the plume region:

$$\mathrm{CE} = \frac{\dot{m}_{\mathrm{C,CO_2}}}{\dot{m}_{\mathrm{C,fuel}}} = \frac{\dot{m}_{\mathrm{C,CO_2}}}{\sum_k \dot{m}_{\mathrm{C},k}} \tag{1}$$

where k represents all the carbon-containing species in the plume, mainly dominated by carbon dioxide (CO_2) and the unburned hydrocarbon (HC) components of the injected fuel stream to the flare stack [23,24]. Carbon mass flow rates are found by multiplying the mass flow rates of carbon-containing species by their corresponding carbon molecular mass fraction. A related parameter, called the destruction removal efficiency (DRE), focuses on a particular species within the fuel stream, such as CH_4, and in cases where the fuel stream is dominated by CH_4, the CE and DRE may be similar. In principle, the mass flow rates in Eq. (1) can be obtained by integrating species mass fluxes along the control surface surrounding the plume region, as demonstrated in Fig. 1. These mass fluxes are the product of volumetric species concentrations and their corresponding projected crosswind velocity, normal to the control surface.

In the case of remote sensing of flare CE, it is often convenient to derive a local (pixel-wise) combustion efficiency based on the ratio of the column number densities of carbon-containing species multiplied by the number of carbon atoms per molecule, $n_{C,k}$. More precisely, for the jth pixel the local CE is expressed as

$$\mathrm{CE}_j = \frac{\sigma_{c,\mathrm{CO_2},j}}{\sum_k n_{\mathrm{C},k}\sigma_{c,k,j}} \tag{2}$$

where $n_{C,k}$ denotes the number of carbon-containing atoms in the kth species. The column number density of the kth species along the jth pixel LOS (molecules/m^2), $\sigma_{c,k,j}$, is

$$\sigma_{c,k,j} = \int_0^L \frac{\chi_{k,j}(s)\,p}{k_{\mathrm{B}}T_j(s)}\,ds \tag{3}$$

where k_B is Boltzmann's constant, $\chi_{k,j}(s)$ and $T_j(s)$ are the mole fraction and temperature profiles at a location s along the jth LOS, and L is the plume width (into the image plane). The atmospheric pressure, p, is taken to be uniform through the plume.

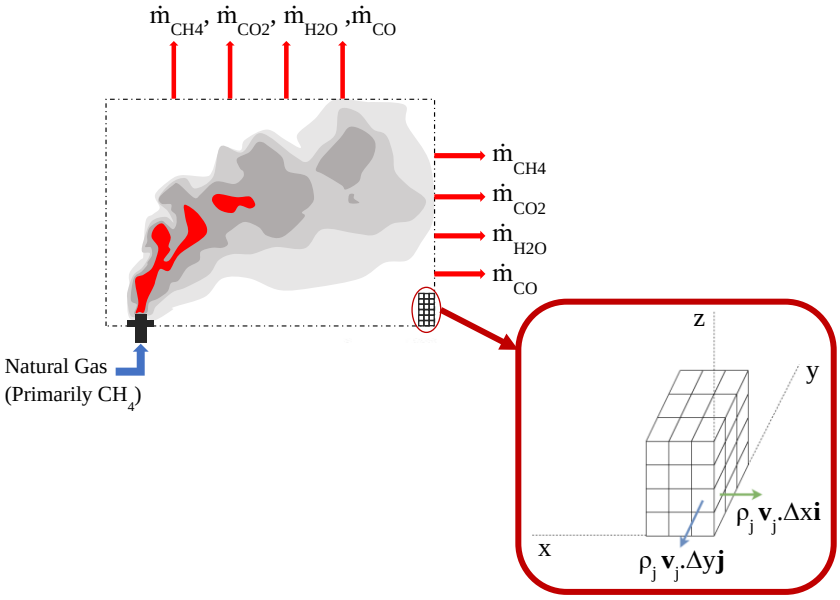

Fig. 1: Obtaining carbon-containing species mass flow rate using mass balance, Eq. , applied to finite elements near the CFD-LES control surface surrounding the plume region, confined by the dashed-dotted line.

The connection between the local CE, Eq. (2), and the global CE, Eq. (1), is not straightforward. Zeng et al. [16,19] suggest that the overall flare CE may be estimated by averaging the local CE of pixels located within an envelope surrounding the combustion zone, rationalizing that these pixels contain gaseous by-products of the complete combustion process. They define the inner envelope surface as the isosurface where the CE increases abruptly in a direction moving outwards from the flame, indicating the completion of the combustion reaction, while the outer surface corresponds to areas with almost undetectable broadband intensity [19].

VISR radiometric model

The species column densities used to compute local CE, Eq. (2), are inferred from a set of captured broadband intensity measurements for each pixel, through a measurement model composed of separated radiometric and instrument sub-models.

Radiometric model

Figure 2 (a) shows a schematic of the radiometric measurement. For simplicity, the present work excludes absorption and emission of the atmospheric layer between the flare and the camera aperture. Since molecular scattering is negligible in the mid-infrared spectrum, the spectral intensity incident on the camera aperture at wavenumber η is given by

$$I_\eta = I_{\eta,\mathrm{bg}} \exp\left[-\int_0^L \kappa_{\eta,\mathrm{mix}}(s)\,ds\right] + \int_0^L \kappa_{\eta,\mathrm{mix}}(s)\, I_{\eta\mathrm{b}}\left[T(s)\right] \exp\left[-\int_s^L \kappa_{\eta,\mathrm{mix}}(s')\,ds'\right] ds \tag{4}$$

where $I_{\eta,\mathrm{bg}}$ is the background irradiation, $I_{\eta,\mathrm{b}}$ is the spectral blackbody emission, L is the plume thickness, $\kappa_{\eta,\mathrm{mix}}$ is the absorption coefficient of the participating gas mixture and $T(s)$ is the plume temperature at a parametric location s along the pixel LOS. The absorption coefficient of the gas mixture is the sum of the absorption coefficients of all participating species at location s along the pixel LOS

$$\kappa_{\eta,\mathrm{mix}}(s) = \sum_k \alpha_{\eta,k}\left(T(s)\right)\sigma_k(s) \tag{5}$$

where σ_k and $\alpha_{\eta,k}$ are the local number density, derived along the corresponding pixel LOS, and the molecular spectral absorption cross-section of the *kth* component inside the plume, respectively. The spectral absorption cross-section can be computed as a function of the local temperature using parameters obtained from the HITRAN database [25].

The incident intensity entering the camera aperture along each pixel LOS is spectrally integrated, e.g., by capturing the scene through a series of spectral broadband filters, projected onto an IR sensor. If the camera contains "top hat" filters that are perfectly transparent over their corresponding detection portions of the mid-wavelength infrared spectrum, and assuming that blackbody emission from the opaque portions is negligible because the filters

are located behind the cold shield of the camera, the signal of the *k*th channel for the *j*th pixel is given by

$$S_{k,j}^{\text{exact}} = C_k \int_{\Delta\eta_k} I_\eta \, d\eta \tag{6}$$

where C_k is a calibration constant that accounts for detector sensitivity, pixel spatial resolution, integration time, and pixel solid angle, and I_η is the spectral intensity, expressed by applying Eq. (4) to the *j*th pixel LOS. In the present analysis, the calibration constants are taken as unity.

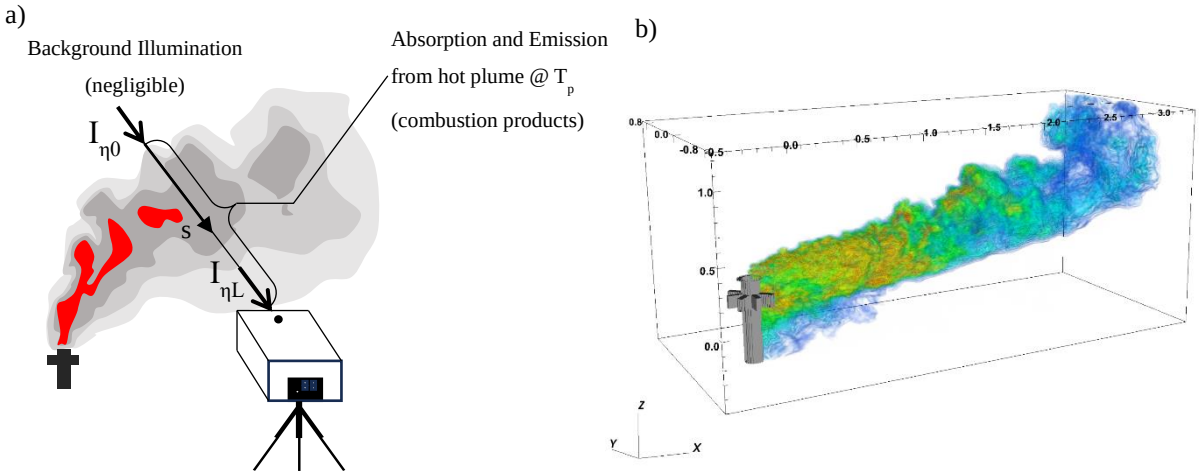

Fig. 2: a) Schematics of the radiometric measurements of the plume using the VISR line-scan hyperspectral camera, b) Sample snapshot of CO_2 mass fraction at t = 11.28 s for CFD-LES Case 1, discussed in Table 1

VISR instrument model implementation

While Eqs. (4)-(6) provide a complete radiometric model of the camera, they cannot be used directly to calculate the quantities needed to derive the local CE, Eq. (2), since the spatial distribution of species and temperature along each LOS is unknown and cannot be inferred from Eq. (4). Moreover, a simpler, computationally inexpensive model is needed to obtain local CE estimates in near real time. Accordingly, Zeng et al. [16] developed an explicit formula for the local CE by assuming: (i) a uniform temperature profile along each pixel LOS (isothermal medium), (ii) an optically thin plume medium (i.e., no self-absorption), (iii) the *k*th channel intensity only corresponds to contributions from the corresponding *k*th carbon-containing species, and (iv) negligible background intensity. Hence, the RTE, Eq. (4), may be rearranged into

$$I_\eta \approx I_{\eta,b}(T)\ \tau_{\eta,L}(T) \tag{7}$$

where the optical thickness, $\tau_{\eta,L}$, is defined according to the Beer-Lambert law,

$$\tau_{\eta,L}(T) = \int_0^L \kappa_{\eta,k}(s)\,ds = \int_0^L \alpha_{\eta,k}\left(T(s)\right) N_k(s)\,ds = \alpha_{\eta,k}(T)\,\sigma_{c,k} \tag{8}$$

If blackbody intensity is approximated as spectrally-uniform over each filter window, the broadband pixel intensity (pixel brightness) for the *k*th channel of the *j*th pixel is expressed by

$$S_{k,j} \approx C_k\,\Delta\eta_k \left\langle I_{\eta_k,b}(T_j)\ \alpha_{\eta,k}(T_j)\right\rangle_{\eta_k} \sigma_{c,k,j} \tag{9}$$

Rearranging for the species column number density, Eq. (3), and substituting the result into Eq. (2) yields the VISR-inferred local CE formula,

$$\text{CE}_j \approx \frac{S_{\text{CO}_2,j} \Big/ \left[C_{\text{CO}_2}\Delta\eta_{\text{CO}_2} \left\langle I_{\eta_{\text{CO}_2},b}(T_j)\,\alpha_{\eta,\text{CO}_2}(T)\right\rangle_{\eta_{\text{CO}_2}} \Big/ n_{\text{C,CO}_2}\right]}{\sum_{k=1}^{3} S_{k,j} \Big/ \left[C_k\Delta\eta_k \left\langle I_{\eta_k,b}(T_j)\,\alpha_{\eta,k}(T)\right\rangle_{\eta_k} \Big/ n_{\text{C},k}\right]} \tag{10}$$

Following Zeng et al. [16], the selected spectral channels are broadly aligned with spectral absorption features of CH_4 (Channel 1, 3.2–3.4 μm), CO_2 (Channel 2, 4.2–4.4 μm), and CO (Channel 3, 4.5–4.9 μm), while the fourth transparent channel is excluded from the analysis. This analysis assumes that the principal flare gas is CH_4 and neglects the radiative contributions of other species over these bands. The effective pixel plume temperature, T_j, influences the

flare local CE estimates through both the absorption line strengths in $\alpha_{\eta,k}$ and the ratio of blackbody intensities of the spectral channels.

Finally, the global CE, Eq. (1), is estimated as the average of local CE values over a sub-region with an inner surface defined by the outer boundary of the flame envelope and an outer surface limited to the region where the observed spectral signal is detectable, above the camera noise threshold (NESR). According to Zeng et al. [19], the inner region may also be approximated by an isotherm surrounding the visible flame boundary. The VISR region-of-interest (ROI) is the zone confined within these two boundaries.

Simulated VISR flare measurements

The VISR technique is assessed using CFD-large eddy simulations of a steam-assisted flare operating in a crosswind. The flare stack has an inner diameter and stack height of 0.08 m and 0.05 m, respectively, and is terminated with a John Zink SKEC© flare tip [26]. Natural gas, composed of 95% methane, 4.5% ethane and 0.5% propane on a molar basis, exits the flare tip with a velocity of 1.2 m/s at 298 K and reacts with a mixture of crosswind ambient air with uniform velocity and assisted by saturated water vapor. Table 1 summarizes the simulation setup configurations, e.g. crosswind and steam assistance flow rates, of the two CFD-LES cases considered in the present analysis. Figure 2 (b) shows a sample snapshot of simulation Case 1, presented in Table 1.

The Uintah-Arches LES solver [22] incorporates a two-stage modelling strategy for turbulent combustion: a slow step using the Westbrook and Dryer reduced-order model [27] for a rate-controlled constrained equilibrium (RCCE) designated to the time-resolved large-scale eddies, and a fast step utilizing instantaneous chemical equilibrium associated with the LES sub-grid scales. Nonequilibrium CO oxidation kinetics are captured using the Dryer and Glassman reduced-order model [28]. Gas phase radiative transfer is modelled using an S_8 discrete ordinates method (DOM) [29], which captures local gas heating or cooling based on the local divergence of the radiative flux. The LES grid, presented in Table 1, initially consists of uniform cubic cells of $8 \times 8 \times 8$ mm^3, which are adapted based on local gradients [21]. The CFD-LES datasets are acquired for at least 72 timesteps in a 5-second simulation time frame.

Table 1: CFD-LES simulation case studies

Case	Crosswind uniform velocity at 298 K (m/s)	Assisted steam mass flow rate at 373 K (g/s)	Total number of cubic elements	CFD-LES domain size (m × m × m)
1	4.2448	10.694	23,581,250	3.92 × 1.76 × 1.75
2	6.9688	86.481	14,175,000	4.0 × 1.08 × 1.68

Simulated temperature and species concentration profiles are then substituted into Eq. (4) to generate spectral intensity, which is then transformed into vectors of the exact broadband data, $\mathbf{b}_{\text{exact}} = [S_1^{\text{exact}}, S_2^{\text{exact}}, S_3^{\text{exact}}]$ via Eq. (6). Finally, the simulated broadband intensities are contaminated with artificial white noise sampled from an unbiased Gaussian distribution characterized by a covariance matrix derived from the prescribed noise equivalent temperature difference (NETD) of 0.035 (mK), typical of the imagers used for VISR [30]:

$$\mathbf{b}^{\text{meas}} = \mathbf{b}^{\text{exact}} + \boldsymbol{\delta}\mathbf{b}^{\text{noise}}, \quad \boldsymbol{\delta}\mathbf{b}^{\text{noise}} \sim \mathcal{N}\left(0, \boldsymbol{\Gamma}_{\text{NETD}}\right) \tag{11}$$

Crucially, the NETD defines the outer detection envelope and limits the camera's ability to resolve pixels containing unheated fuel that has been aerodynamically stripped from the combustion zone.

In their experimental analysis, Zeng et al. [19] averaged 325 data cubes temporally to reduce the number of data sets that would need to be processed analytically, although this would also improve the signal-to-noise (S/N) ratio. We explore this effect by averaging temporally resolved synthetic images over approximately 5 seconds (72 timesteps), resulting in an extended region of detected intensity across all the VISR spectral bins.

A noise threshold is introduced to the simulated broadband images, based on the overall net equivalent spectral radiance (NESR) value. The implemented noise threshold filters out the pixels with a low S/N ratio, depicted by the white region in Fig. 3. This effect is most pronounced for the CH_4 and CO channels in high and low flare CE scenarios, respectively, since it coincides with the lowest abundance, temperature, and species concentration in the flare plume. In principle, the finite dynamic range of the camera likely means that some pixels in the combustion zone may also be saturated, although this effect is not considered here.

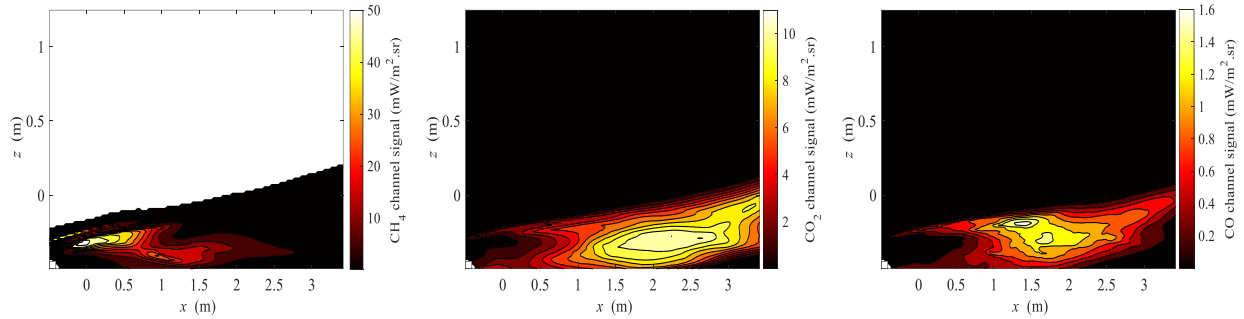

Fig. 3: Synthetic time-averaged broadband images corresponding to the spectral bins of the VISR camera for case 2: (a) CH_4 (3.2–3.4 μm), (b) CO_2 (4.2–4.4 μm), and (c) CO (4.5–4.9 μm). The white region represents pixels with undetectable signals reaching over the noise threshold (below the NESR).

Results and Discussion

We first assess the validity of the simplified radiometric model. Two key simplifications made to derive the simplified VISR model are the optically thin approximation, and that the temperature and species concentrations are distributed uniformly along each pixel LOS. Figure 4 demonstrates sample 2D contours of the inferred and ground truth local CE for Case 1, presented in Table 1, at an arbitrary timestep. The local CE relative error, demonstrated in Fig. 4 (c), is defined as the local CE error relative to the mean ground truth local CE of the pixels located within the VISR ROI. For most of the VISR ROI pixels, this error is generally less than 2%. A similar agreement was observed for the other crosswind scenario, with considerably much larger local CE relative errors within the flame envelope, representing the active combustion zone for both simulation cases. This indicates that the simplifications applied to the RTE in the VISR radiometric model could potentially yield reasonable outcomes, which are ultimately converted to accurate local CE estimates.

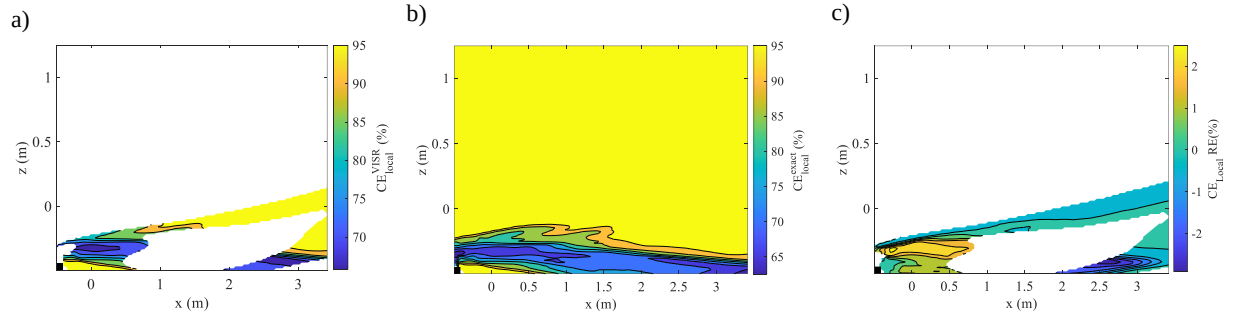

Fig. 4: Sample 2D contours of local CE: a) inferred using VISR instrument model, Eq. (10), b) ground-truth (CFD-driven), Eq. (2), along with c) corresponding local CE relative error, for simulation case 1, presented in Table 1, at an arbitrary timestep. The white zone is indicative of the VISR ROI containing pixels with incident spectral intensity below the noise (NESR) threshold of the VISR camera (surrounding the plume), excluding the flame envelope, representing the combustion zone, approximated by the visible flame.

To fully assess the VISR instrumentational model, an uncertainty analysis is conducted on the robustness of the VISR flare CE averaging model. This analysis compares time-resolved (instantaneous) flare global CE estimates, computed as the mean VISR-inferred local CE of the pixels located within the VISR ROI, with their corresponding ground truth (benchmark) values, obtained by substituting the CFD-driven temperature and species concentration fields in Eq. (1). According to Fig. 5, the VISR generally tends to underestimate the flare CE compared to the respective ground truth, whereas the error, the difference between the global CE VISR predictions and ground truth, is more pronounced for Case 1, Fig. 5 (a), with less steam-assistance and lower crosswind velocity.

The final aspect in evaluating the effectiveness of the VISR approach for remote monitoring of the flare operations is its ability to detect fugitive cold methane that is removed from the combustion cone via aerodynamic stripping [5,6]. Figure 6 (a) shows three transects, selected across the VISR ROI, which shows the plume temperature and methane

mass flux (kg/m.s) profiles. According to Fig. 6 (b), there is a considerable amount of stripped methane at low temperatures, downstream of the plume under the flare stack level, which is separated from the rest of the fugitive methane by the horizontal dashed line. Moreover, methane mass flux profiles in Fig. 6 (c) show negligible evidence of the stripped methane existence, along the two transects located between the flare stack and the flame envelope, representing the combustion zone. For the other CFD-LES scenario with higher crosswind conditions, similar behaviour regarding the distribution of stripped methane flux downstream of the plume below the flare stack level, was observed. The existence of the region with an abundance of stripped (cold) methane concentration, outside the VISR detection zone (ROI), Fig. 6 (b), highlights the VISR instrument's shortcomings in terms of cold (stripped) methane detection. According to the results, the VISR technique can capture less than 25% of the overall stripped methane mass flux in simulation Case 1, shown in Table 1. Furthermore, this figure is expected to be smaller for higher crosswind conditions, with generally more presence of stripped cold methane, e.g. only around 12% of the stripped methane mass flux is detectable by the VISR imager for Case 2, presented in Table 1. Subsequently, this limitation can directly impact the accuracy of flare CE estimates by underpredicting the methane concentration, used in the inferred local CE, Eq. (10), resulting in an overestimated flare CE by the VISR approach. Overall, such overpredictions of flare performance are expected to be more prominent for the higher crosswind conditions.

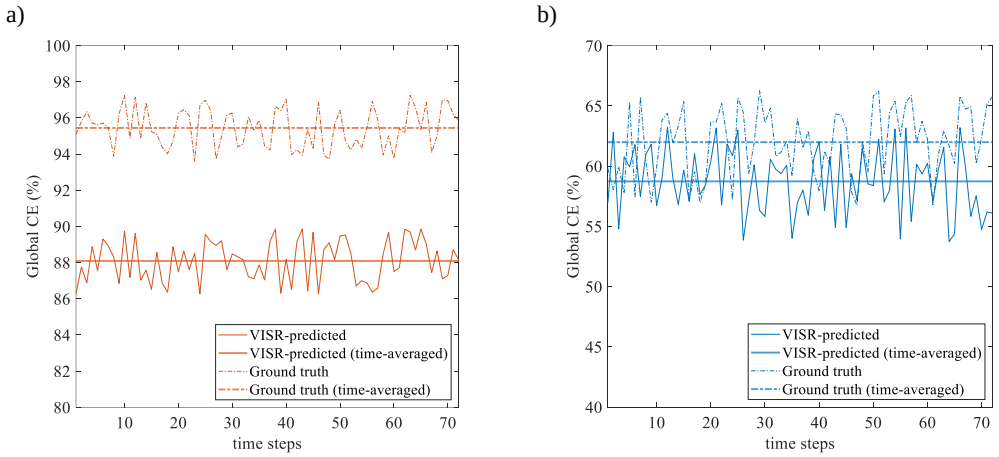

Fig. 5: Time-resolved (instantaneous) VISR global CE predictions vs. ground truth (CFD-driven) global CE, paired with their corresponding time-averaged values, in a span of 5 seconds (72 timesteps), for simulation: a) case 1, and b) case 2, shown in Table 1.

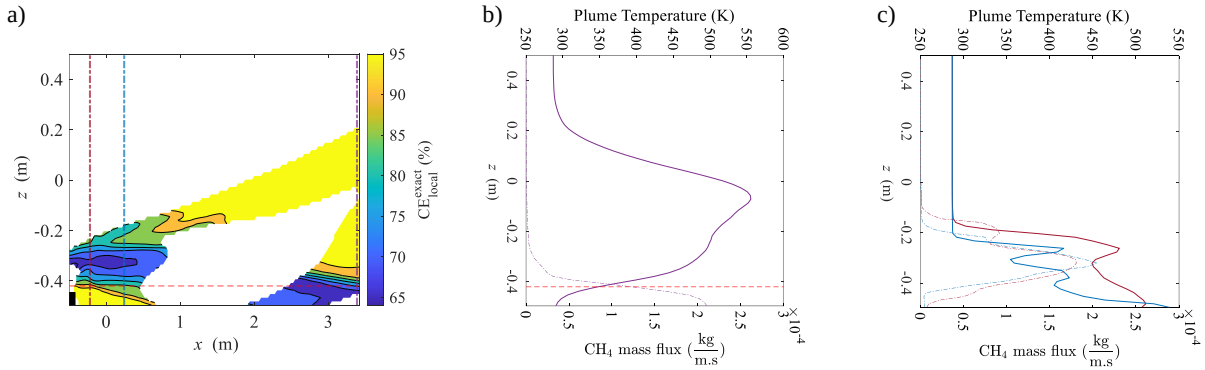

Fig. 6: VISR instrument capabilities for the detection of stripped (cold) methane: a) 2D contour of VISR-inferred local CE at an arbitrary time step for case 1, presented in Table 1. Vertical dashed lines represent the three selected transects, located within the VISR ROI. The inferred plume temperature (solid line) and methane mass flux (dashed line) along the illustrated transects, b) located at the edge of the combustion zone and c) between the flare stack and the combustion zone. The red dashed line separates the region with an abundance of unburned methane, downstream of the plume (VISR ROI), from the hotter and more sparse fugitive methane.

Conclusions

Video imaging spectro-radiometry (VISR) has recently been proposed as a means for continuous monitoring of flare combustion efficiency (CE), but the assumptions and simplifications that underlie this technique have yet to be tested rigorously. This analysis is conducted on a simplified version of the VISR approach, based on three spectral channels aligned with key absorption features of CO_2 (4.2–4.4 μm), CO (4.5–4.9 μm), and CH_4 (3.2–3.4 μm). Synthetic broadband images for the VISR spectral channels are generated using computational fluid dynamics simulations of a steam-assisted industrial flare, operating in varying crossflow conditions.

Current analysis of the VISR local CE inference model supports the simplifications, applied to the radiative transfer equation (RTE) in the VISR radiometric model, for pixels located within the VISR region-of-interest (ROI). Reasonable agreement between the inferred local CE and their corresponding ground truth, with the relative error typically less than 2% of the ground truth, supports the utilization of the current VISR instrument model for estimating the local CE of the pixels located within the VISR ROI. Conversely, in contrast to the ground truth, the results suggest an overestimation tendency in the VISR global CE predictions, particularly for the flaring processes operating in lower crosswind conditions. This fact, combined with the VISR MWIR instrument's lack of reliability for detecting fugitive pockets of unburned cold methane, created due to the aerodynamic fuel-stripping mechanism, results in biased flare CE quantifications.

Finally, we wish to emphasize that, in our estimation, the VISR technique should be able to detect unfavorable operating conditions (e.g., over-assisted flares) and, in this context, might be a very useful tool for the oil and gas industry to reduce emissions caused by inefficient flaring. We also note that our study was conducted on a simplified version of the commercial VISR product, incorporating the details disclosed in the original patent. The commercial version of this technology offers a significantly higher degree of spectral resolution and more complex algorithms through which the broadband images are converted into a global CE estimate, which are not fully known. Nevertheless, in our opinion, this analysis does not support the statements regarding the accuracy of this approach for quantifying flare CE.

References

[1] IPCC, AR5 climate change 2013: The physical science basis. IPCC, 2024. https://www.ipcc.ch/report/ar5/wg1/ (accessed April 30, 2024).

[2] World Bank, Zero Routine Flaring by 2030, (2015). https://www.worldbank.org/en/programs/zero-routine-flaring-by-2030 (accessed April 30, 2024).

[3] Environment and Climate Change Canada, Reducing methane emissions from Canada's oil and gas sector: discussion paper, 2022. https://www.canada.ca/en/environment-climate-change/services/canadian-environmental-protection-act-registry/consultation-reducing-methane-emissions-oil-gas-sector.html (accessed July 1, 2024).

[4] World Bank, Global Gas Flaring Reduction Partnership (GGFR). World Bank., (2022). https://www.worldbank.org/en/programs/gasflaringreduction/global-flaring-data (accessed April 30, 2024).

[5] M.R. JOHNSON, D.J. WILSON, L.W. KOSTIUK, A FUEL STRIPPING MECHANISM FOR WAKE-STABILIZED JET DIFFUSION FLAMES IN CROSSFLOW, Combustion Science and Technology 169 (2001) 155–174. https://doi.org/10.1080/00102200108907844.

[6] V.M. Torres, S. Herndon, Z. Kodesh, D.T. Allen, Industrial Flare Performance at Low Flow Conditions. 1. Study Overview, Ind Eng Chem Res 51 (2012) 12559–12568. https://doi.org/10.1021/ie202674t.

[7] V.M. Torres, S. Herndon, D.T. Allen, Industrial Flare Performance at Low Flow Conditions. 2. Steam- and Air-Assisted Flares, Ind Eng Chem Res 51 (2012) 12569–12576. https://doi.org/10.1021/ie202675f.

[8] A. Ahsan, H. Ahsan, J.S. Olfert, L.W. Kostiuk, Quantifying the carbon conversion efficiency and emission indices of a lab-scale natural gas flare with internal coflows of air or steam, Exp Therm Fluid Sci 103 (2019) 133–142. https://doi.org/10.1016/j.expthermflusci.2019.01.013.

[9] M. Zamani, E. Abbasi-Atibeh, S. Mobaseri, H. Ahsan, A. Ahsan, J.S. Olfert, L.W. Kostiuk, An experimental study on the carbon conversion efficiency and emission indices of air and steam co-flow diffusion jet flames, Fuel 287 (2021) 119534. https://doi.org/10.1016/j.fuel.2020.119534.

[10] M.R. Johnson, L.W. Kostiuk, Efficiencies of low-momentum jet diffusion flames in crosswinds, Combust Flame 123 (2000) 189–200. https://doi.org/10.1016/S0010-2180(00)00151-6.

[11] D.T. Allen, D. Smith, V.M. Torres, F.C. Saldaña, Carbon dioxide, methane and black carbon emissions from upstream oil and gas flaring in the United States, Curr Opin Chem Eng 13 (2016) 119–123. https://doi.org/10.1016/j.coche.2016.08.014.

[12] T.R. Blackwood, An Evaluation of Flare Combustion Efficiency Using Open-Path Fourier Transform Infrared Technology, J Air Waste Manage Assoc 50 (2000) 1714–1722. https://doi.org/10.1080/10473289.2000.10464206.

[13] A. Soufiani, J.P. Martin, J.C. Rolon, L. Brenez, Sensitivity of temperature and concentration measurements in hot gases from FTIR emission spectroscopy, J Quant Spectrosc Radiat Transf 73 (2002) 317–327. https://doi.org/10.1016/S0022-4073(01)00209-6.

[14] J. Wormhoudt, S.C. Herndon, J. Franklin, E.C. Wood, B. Knighton, S. Evans, C. Laush, M. Sloss, R. Spellicy, Comparison of Remote Sensing and Extractive Sampling Measurements of Flare Combustion Efficiency, Ind Eng Chem Res 51 (2012) 12621–12629. https://doi.org/10.1021/ie202783m.

[15] C. Hahne, A. Aggoun, V. Velisavljevic, S. Fiebig, M. Pesch, Refocusing distance of a standard plenoptic camera, Opt Express 24 (2016) 21521. https://doi.org/10.1364/OE.24.021521.

[16] Y. Zeng, J. Morris, M. Dombrowski, Multi-spectral infrared imaging system for flare combustion efficiency monitoring, US 9258495 B2, 2012. https://patents.google.com/patent/US9258495B2/en (accessed April 23, 2024).

[17] R.B. Miguel, S. Talebi-Moghaddam, M. Zamani, C. Turcotte, K.J. Daun, Assessing flare combustion efficiency using imaging Fourier transform spectroscopy, J Quant Spectrosc Radiat Transf 273 (2021) 107835.

[18] M. Gålfalk, G. Olofsson, D. Bastviken, Approaches for hyperspectral remote flux quantification and visualization of GHGs in the environment, Remote Sens Environ 191 (2017) 81–94. https://doi.org/10.1016/J.RSE.2017.01.012.

[19] Y. Zeng, J. Morris, M. Dombrowski, Validation of a new method for measuring and continuously monitoring the efficiency of industrial flares, J Air Waste Manage Assoc 66 (2016) 76–86. https://doi.org/10.1080/10962247.2015.1114045.

[20] S. Smith, J.M. Miskelly, NEW DIRECT FLAME MONITORING TECHNOLOGY, 2021. https://collections.lib.utah.edu/ark:/87278/s6rg0507 (accessed April 23, 2024).

[21] Jebin Elias, DEVELOPMENT OF A DIGITAL TWIN FOR INDUSTRIAL METHANE FLARES GROUNDED ON THE PRINCIPLES OF BAYESIAN INFERENCE, University of Utah, 2024.

[22] A. Jatale, P.J. Smith, J.N. Thornock, S.T. Smith, M. Hradisky, A Validation of Flare Combustion Efficiency Predictions From Large Eddy Simulations, J Verif Valid Uncertain Quantif 1 (2016) 21001. https://doi.org/10.1115/1.4031141.

[23] D.J. Corbin, M.R. Johnson, Detailed Expressions and Methodologies for Measuring Flare Combustion Efficiency, Species Emission Rates, and Associated Uncertainties, Ind Eng Chem Res 53 (2014) 19359–19369. https://doi.org/10.1021/ie502914k.

[24] P. Poudenx, Plume sampling of a flare in crosswind: structure and combustion efficiency, 2000. https://doi.org/https://doi.org/10.7939/R3QN5ZG34.

[25] I.E. Gordon, L.S. Rothman, R.J. Hargreaves, R. Hashemi, E.V. Karlovets, F.M. Skinner, E.K. Conway, C. Hill, R.V. Kochanov, Y. Tan, P. Wcisło, A.A. Finenko, K. Nelson, P.F. Bernath, M. Birk, V. Boudon, A. Campargue, K.V. Chance, A. Coustenis, B.J. Drouin, J. –M. Flaud, R.R. Gamache, J.T. Hodges, D. Jacquemart, E.J. Mlawer, A.V. Nikitin, V.I. Perevalov, M. Rotger, J. Tennyson, G.C. Toon, H. Tran, V.G. Tyuterev, E.M. Adkins, A. Baker, A. Barbe, E. Canè, A.G. Császár, A. Dudaryonok, O. Egorov, A.J. Fleisher, H. Fleurbaey, A. Foltynowicz, T. Furtenbacher, J.J. Harrison, J. –M. Hartmann, V. –M. Horneman, X. Huang, T. Karman, J. Karns, S. Kassi, I. Kleiner, V. Kofman, F. Kwabia–Tchana, N.N. Lavrentieva, T.J. Lee, D.A. Long, A.A. Lukashevskaya, O.M. Lyulin, V.Yu. Makhnev, W. Matt, S.T. Massie, M. Melosso, S.N. Mikhailenko, D. Mondelain, H.S.P. Müller, O.V. Naumenko, A. Perrin, O.L. Polyansky, E. Raddaoui, P.L. Raston, Z.D. Reed, M. Rey, C. Richard, R. Tóbiás, I. Sadiek, D.W. Schwenke, E. Starikova, K. Sung, F. Tamassia, S.A. Tashkun, J. Vander Auwera, I.A. Vasilenko, A.A. Vigasin, G.L. Villanueva, B. Vispoel, G. Wagner, A. Yachmenev, S.N. Yurchenko, The HITRAN2020 molecular spectroscopic database, J Quant Spectrosc Radiat Transf 277 (2022) 107949. https://doi.org/10.1016/j.jqsrt.2021.107949.

[26] R.E. Schwartz, M.R. Keller, Apparatus and method to add kinetic energy to a low pressure waste gas flare burner, 1987. https://www.osti.gov/biblio/6874701.

[27] C.K. WESTBROOK, F.L. DRYER, Simplified Reaction Mechanisms for the Oxidation of Hydrocarbon Fuels in Flames, Combustion Science and Technology 27 (1981) 31–43. https://doi.org/10.1080/00102208108946970.

[28] F.L. Dryer, I. Glassman, High-temperature oxidation of CO and CH4, Symposium (International) on Combustion 14 (1973) 987–1003. https://doi.org/10.1016/S0082-0784(73)80090-6.

[29] M.F. Modest, S. Mazumder, The Method of Discrete Ordinates (<math altimg="si1.svg"> <msub> <mrow> <mtext mathvariant="italic">S</mtext> </mrow> <mrow> <mtext mathvariant="italic">N</mtext> </mrow> </msub> </math> -Approximation), in: Radiative Heat Transfer, Elsevier, 2022: pp. 563–616. https://doi.org/10.1016/B978-0-12-818143-0.00024-9.

[30] C. Surface Optics, SOC750 Midwave Infrared Hyperspectral Imager, (2021). https://surfaceoptics.com/products/hyperspectral-imaging/soc750/ (accessed April 24, 2024).